Energy Advances

ROYAL SOCIETY OF CHEMISTRY

PAPER

View Article Online
View Journal | View Issue

Cite this: *Energy Adv.*, 2025, 4, 1345

First-principles calculation of a 1T-VS_2/graphene composite as a high-performance anode material for lithium- and sodium-ion batteries

Ahmed Jaber Hassan, [bd] Kar Tim Chan, [*ab] Kean Pah Lim, [b] Nurisya Mohd Shah, [ab] Umair Abdul Halim, [c] Nurfarhana Mohd Noor [b] and Wan Mohammad Zulkarnain Abdul Razak [b]

Graphene and other conductive substrates have been used to improve the electrochemical efficiency of monolayer VS_2, establishing it as a potential anode material for LIBs. Nonetheless, a detailed understanding of the synergistic relationship between VS_2 and graphene (Gr), which is fundamental for boosting Li^+/Na^+ electrochemical storage device performance, remains limited. This study utilized density functional theory (DFT) computations to systematically analyze the VS_2/Gr composite as an optimized electrode for Li^+/Na^+ electrochemical storage devices. Our findings reveal that VS_2/Gr possesses outstanding structural stability, remarkable mechanical stiffness, strong ion adsorption ability, and enhanced charge transfer efficiency. Additionally, it exhibits a high theoretical storage capacity, a shallow average open-circuit voltage, and low ion diffusion barriers. The diffusion barriers of 0.11 eV for Li and 0.16 eV for Na are lower than those of widely studied composite materials, enabling an exceptionally fast Li^+/Na^+ diffusion rate during charge/discharge processes. The predicted open-circuit voltages for Li^+/Na^+ are 0.75 V and 0.77 V, respectively, with corresponding theoretical storage capacities reaching 1156 mAh g^{-1} for Li and 770 mAh g^{-1} for Na. These findings offer key insights for the experimental design and optimization of VS_2/Gr anodes, paving the way for ultra-fast charging and high-capacity Li^+/Na^+ electrochemical storage devices.

Received 8th May 2025,
Accepted 26th August 2025

DOI: 10.1039/d5ya00110b

rsc.li/energy-advances

1. Introduction

The growth of the global population has led to increased energy demands and environmental challenges, necessitating urgent action in energy consumption and environmental protection. Energy, a fundamental pillar of modern civilization, is predominantly sourced from fossil fuels, which contribute significantly to global warming and environmental degradation. By 2050, global energy demand is projected to reach 27.6 TW.[1–3] To mitigate these challenges, researchers are focusing on renewable energy sources and advanced energy storage technologies, including supercapacitors, batteries, solar cells, and hydrogen generation through water splitting.[1,4,5] Among these, lithium-ion batteries (LIBs) are esteemed for their elevated energy density, extended cycle life, less self-discharge among diverse energy storage systems, and minimal environmental impact.[6–8] LIBs are extensively used in electric vehicles, portable electronics, medical devices, and aerospace technologies.[9] However, despite these advantages, graphite, the conventional LIB anode material, has a limited theoretical storage capacity of approximately 372 mAh g^{-1} and exhibits low energy density, poor cycling stability, and voltage hysteresis.[9–11] Additionally, limited global lithium reserves and increasing demand raise sustainability concerns.[7,12] Sodium-ion batteries (SIBs) have garnered attention as an alternative owing to the abundant availability of sodium, cost-effective production, and enhanced safety. However, the larger ionic radius of Na^+ results in slower intercalation/deintercalation, leading to reduced capacity and rate performance.[10] These obstacles have fueled significant research aimed at discovering advanced negative electrode materials for Li^+/Na^+ electrochemical storage devices.[9] Among the most promising candidates, graphene, transition metal dichalcogenides (TMDs) like MoS_2 and VS_2, and MXenes, have demonstrated outstanding electrical conductivity, high charge storage capacity, and exceptional rate performance as promising two-dimensional (2D) materials.[9,13,14] Nevertheless, finding

[a] *Institute for Mathematical Research (INSPEM), Universiti Putra Malaysia (UPM), 43400 UPM Serdang, Selangor Darul Ehsan, Malaysia. E-mail: chankt@upm.edu.my*
[b] *Department of Physics, Faculty of Science, Universiti Putra Malaysia (UPM), 43400 UPM Serdang, Selangor Darul Ehsan, Malaysia*
[c] *Centre of Foundation Studies for Agricultural Science, Universiti Putra Malaysia (UPM), 43400 UPM Serdang, Selangor Darul Ehsan, Malaysia*
[d] *Department of Physics, College of Science, University of Thi-Qar, Nasiriya, Iraq*

an optimal negative electrode material that harmonizes these properties continues to be a challenge.[15] Composites, constructed by stacking 2D materials, offer a synergistic approach to enhance anode properties by combining the strengths of individual materials while minimizing their weaknesses through van der Waals interactions. Graphene, widely used as a conductive substrate, enhances particle contact and reduces volume expansion/shrinkage during charge cycles, improving overall stability.[15–18] Several graphene-based composites, including MoS_2/graphene and WS_2/graphene, have demonstrated excellent electrochemical performance, making them promising candidates for metal–ion battery applications.[19–21] Among TMDs, vanadium disulfide (VS_2) has attracted significant attention due to its applications in sensing, catalysis, and energy storage.[22,23] The VS_2/graphene hybrids are particularly promising as an anode for LIBs, demonstrating great capacity, exceptional cycling stability, and amazing rate capability.[8,24] The strong interaction between VS_2 and graphene enhances electron transport and mechanical stability, improving overall electrochemical performance. For instance, Ma *et al.* demonstrated that VS_2 nanosheets/graphene composites, when used as anodes in LIBs, deliver high reversible capacity, superior rate performance, and excellent cycling stability.[25] Similarly, He *et al.* developed hollow VS_2@reduced graphene oxide (RGO) structures *via* a solvothermal method, achieving outstanding electrochemical performance in sodium-ion batteries, including high reversible discharge capacity and prolonged cycle life.[26] Despite these advantages, the potential of the VS_2/graphene composite structure (VS_2/Gr) for sodium-ion batteries (SIB) remains underexplored. Additionally, the mechanical characteristics, energy storage capabilities, and Li-ion and Na-ion transport processes require further investigation. This work performs first-principles simulations to investigate the VS_2/Gr composite as a negative electrode material for Li/Na-ion storage devices. We systematically examine its structural stability, electrical characteristics, and mechanical performance, Li^+/Na^+ diffusion barriers, average open-circuit voltage, and specific capacity. By gaining a deeper insight into the energy storage and ion transport mechanisms, this work aims to optimize the VS_2/graphene composite, establishing it as a key material for high-performance LIBs and SIBs.

2. Computational details

The computations were performed utilizing the Quantum ESPRESSO software program.[27] The exchange–correlation functional was evaluated using the generalized gradient approximation (GGA) as formulated by Perdew, Burke, and Ernzerhof (PBE) in 1996.[28] Crystal structures were visualized using the VESTA program.[29] Density functional theory (DFT) computations have been utilized to optimize the atomic configurations and analyze their electronic, mechanical, and electrochemical characteristics. For the VS_2/graphene composite structure, a $(2 \times 2 \times 1)$ VS_2 monolayer supercell was positioned over a $(\sqrt{7} \times \sqrt{7} \times 1)$ graphene supercell, resulting in a lattice mismatch of approximately 0.17%. A vacuum gap of 17 Å was implemented along the *z*-axis to inhibit interlayer interactions. The self-consistent field (SCF) calculations were conducted with an energy convergence threshold of 1.0×10^{-9} Ry, utilizing a $(6 \times 6 \times 1)$ *k*-point mesh following the Monkhorst–Pack technique. For the ultra-soft pseudopotential, the required kinetic energy cutoff for the charge density (ecutrho) was set to eight times the kinetic energy cutoff for the wave function (ecutwfc). Considering the weak van der Waals (vdW) attractions in the VS_2/Gr composite, the vdW-D2 scheme by Grimme[30] was applied to account for dispersion corrections. Additionally, spin-polarized calculations were also conducted. The thermodynamic stability of the VS_2/Gr composite was evaluated by calculating its formation energy (ΔH_f) using the following equation:[31,32]

$$\Delta H_f = E_{system} - \sum_i N_i \mu_i \quad (1)$$

where ΔH_f is the formation energy, E_{system} signifies the DFT total energy calculated for the proposed composite, N_i represents the total number of atom species, and μ_i represents the chemical potential of the atom, obtained from its bulk phase. The chemical potential of the atoms was derived from their bulk phases. To assess the mechanical properties, the in-plane stiffness (Y_{2D}) of the 2D materials was calculated to assess their rigidity and flexibility. The in-plane stiffness is derived using the following formula:[33–36]

$$Y_{2D} = (1/A_0)(\partial^2 E_s/\partial \varepsilon^2) \quad (2)$$

Here, E_s represents the strain energy (computed by eqn (3)), A_0 is the equilibrium area of the relaxed structure, and $\varepsilon = (a - a_0)/a_0$ is an in-plane uniaxial strain, where a_0 and a are the lattice parameters before and after stretching, respectively. The strain energy E_s is computed as:

$$E_s = (E_{tot} - E_0)/n \quad (3)$$

where E_{tot} is the total energy of the strained system and E_0 is the total energy of the unstrained system (at zero applied strain). To analyze Li^+/Na^+ mobility, the climbing image nudged elastic band (CI-NEB) method was employed to calculate the diffusion barriers, utilizing a high-throughput computational platform specifically designed for battery materials.[37] The diffusion coefficient (D) was assessed using the following equation:[15]

$$D = l^2 \nu \exp(-E_a/k_B T) \quad (4)$$

where l^2 denotes the ion diffusion distance, E_a represents the activation energy barrier, T indicates the absolute temperature (set at 300 Kelvin), k_B corresponds to the Boltzmann constant (8.617×10^{-5} eV K^{-1}), and ν represents the attempt frequency (10^{13} Hz).

3. Results and discussion

3.1 Geometry

Three stacking configurations: AA, AB, and BA, were examined for the VS_2/graphene heterostructure, as shown in Fig. 1. These

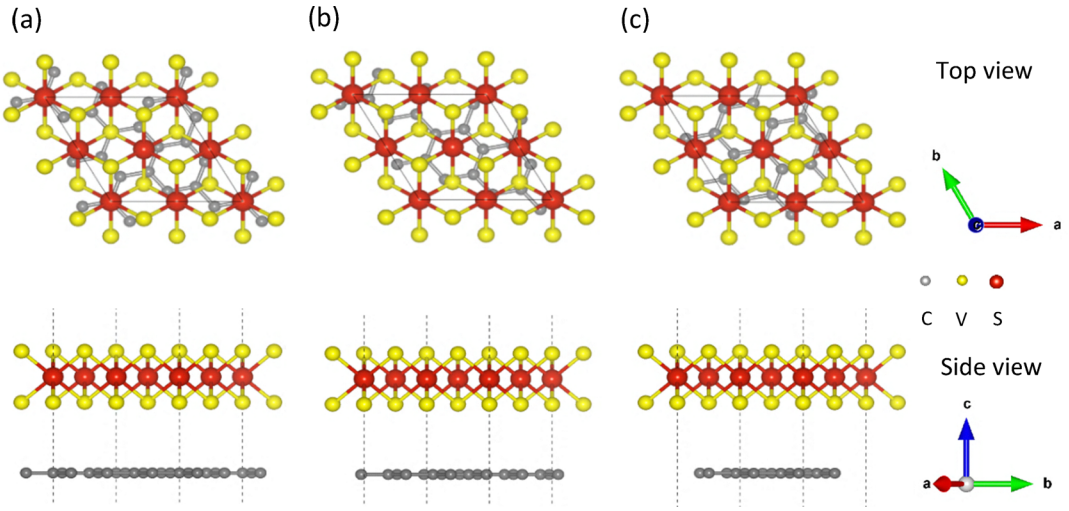

Fig. 1 Top and side views of the three interfacial stacking configurations of the VS_2/graphene heterobilayer: (a) AA stacking, (b) AB stacking, and (c) BA stacking.

configurations reflect different lateral alignments between the layers, influencing interfacial interactions, structural stability, and bonding strength. Formation energies were calculated using eqn (1) to determine the most favorable stacking arrangement for the VS_2/graphene heterostructure. All configurations: AA, AB, and BA, exhibited negative formation energies (−0.011 eV, −0.010 eV, and −0.010 eV, respectively), confirming their thermodynamic stability. Among them, the AA stacking configuration had the lowest formation energy, indicating that it is the most stable interfacial arrangement. Consequently, the structural optimization was performed based on the AA stacking mode, resulting in optimized lattice parameters of $a = b = 6.494$ Å and an equilibrium interlayer distance of 3.96 Å between the VS_2 and graphene layers. These values align closely with previously reported theoretical results for the 2D graphene-based composites, which exhibit interlayer distances in the range from 3.30 to 4.2 Å.[7,15,38–40] The VS_2/Gr composite structure contains 14 carbon (C) atoms from graphene, eight sulfur (S) atoms, and four vanadium (V) atoms from the VS_2 monolayer, as depicted in Fig. 2.

Notably, the monolayer VS_2 completely covers the graphene substrate without significantly altering its geometry, as depicted in Fig. 2. This is due to the minimal lattice mismatch (0.17%) between the VS_2 and graphene structures. The computed formation energy of the VS_2/Gr composite is −0.011 eV, indicating that the composite is thermodynamically stable and its formation is energetically favorable. A negative formation energy confirms that the VS_2 monolayer successfully integrates with the graphene monolayer, forming a stable composite, whereas a positive ΔH_f would indicate an endothermic process and thermodynamically unstable structures.[41]

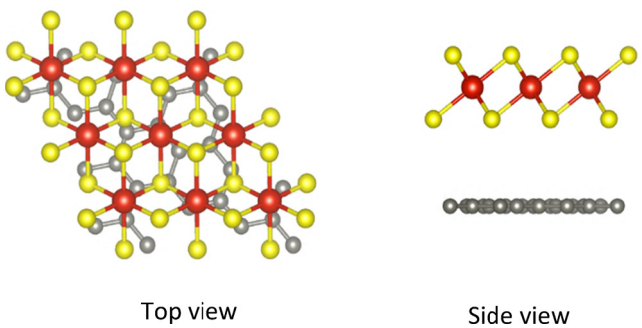

Fig. 2 Diagram of the composite configuration of the VS_2/Gr composite structure. The gray, blue, red, and yellow spheres correspond to carbon (C), vanadium (V), and sulfur (S) atoms, respectively.

3.2 Electronic properties

Electrical conductivity is crucial for enhancing the charge/discharge performance of anode materials in Li-ion and Na-ion batteries. The VS_2/Gr composite exhibits metallic behavior with highly electrical conductivity, as illustrated in Fig. 3a. Owing to weak van der Waals contacts between the graphene and VS_2, the Dirac cone of graphene remains intact at the Dirac (K) point, indicating that the graphene retains its unique electronic properties. The Fermi level (E_f) represented by the dashed line intersects multiple bands, confirming the metallic nature of the composite. This observation is consistent with prior studies that highlight the metallic characteristics of VS_2/graphene composites.[40,42,43] According to the projected density of states (PDOS) in Fig. 3b, the d-orbitals of vanadium atoms significantly contribute near the Fermi level, serving as a key factor in enhancing electrical conductivity. A high DOS at E_f indicates the presence of readily available electronic states, facilitating efficient charge transport. Conversely, the p-orbitals of sulphur and carbon (graphene) atoms are predominantly filled below the Fermi level, constituting the valence band and contributing less to electrical conduction. The internal S-p and Gr-p orbitals exhibit a lower density of states and are positioned energetically farther from E_f, indicating their minimal contribution to conductivity. The strong presence of V-d and S-p orbitals near E_f ensures a high density of mobile charge carriers, thereby enhancing the electronic conductivity

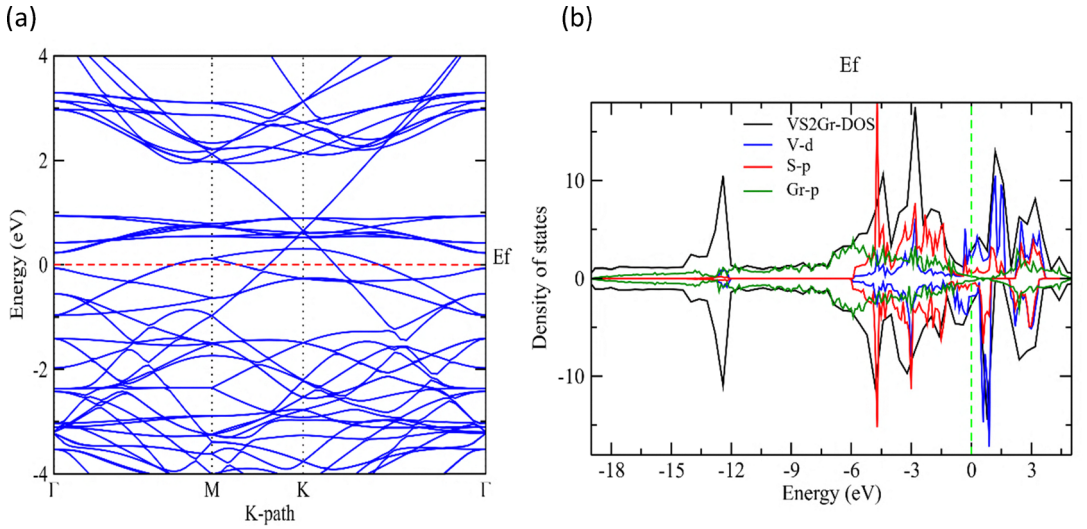

Fig. 3 (a) The band structure and (b) density of states (DOS) of the VS_2/Gr composite, with the dashed line indicating the Fermi level (E_f).

of the VS_2/Gr heterostructure. This makes it a promising high-performance anode material for next-generation Li-ion (LIBs) and Na-ion (SIBs) batteries.

3.3 Mechanical properties

The mechanical stability of an anode material is crucial for maintaining long-term battery cycling performance. Structural deformation or pulverization of electrodes can lead to rapid capacity decline and degradation and reduced cycling stability. Therefore, an efficient negative electrode material must possess exceptional mechanical strength and stretchability to withstand volume expansion during Li^+/Na^+ insertion and extraction cycles. To evaluate the mechanical properties of the VS_2/Gr composite, we conducted density functional theory (DFT) simulations to identify its elastic constants and in-plane stiffness.

3.3.1 Elastic properties. For 3D materials, the elasticity properties are often characterized by Young's modulus (Y). However, since monolayers lack a defined thickness, the in-plane stiffness (Y_{2D}) is a more appropriate measure of mechanical strength for 2D materials.[34] A hexagonal supercell with x and y axes along the armchair and zigzag directions, was used to compute the elastic constants of the composites. The system was subjected to biaxial strain (ε) by varying the lattice constants from −2% to 2% in increments of 1.0%, allowing full relaxation of atomic positions in-plane as shown in Fig. 4a. A data matrix of 25 strain configurations was generated by applying two sets of strain conditions along the x and y directions. For each strain condition, the total energy was optimized, resulting in a detailed energy-strain dataset of 225 points (Fig. 4b). The strain energy (E_s) was fitted using a polynomial model, given by:

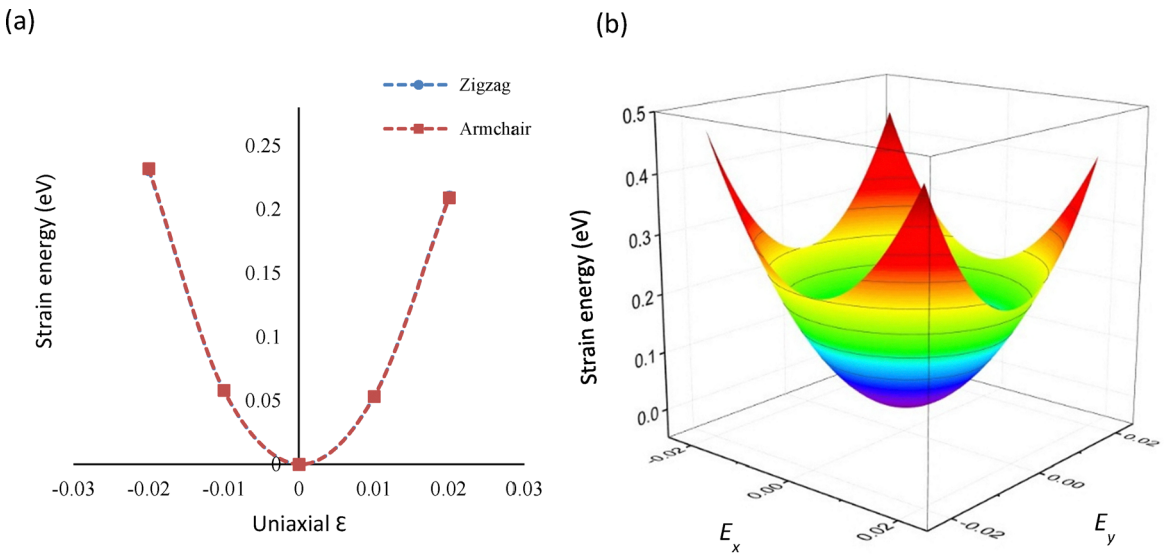

Fig. 4 Structural and mechanical response of the 2D VS_2/Gr composite under uniform expansion: (a) uniaxial strain energy-strain curves along the armchair and zigzag directions and (b) 3D fitted surface plot of total energy as a function of elastic strain.

$$E_s = b_1\varepsilon_x^2 + b_2\varepsilon_y^2 + b_3\varepsilon_x\varepsilon_y \quad (5)$$

where ε_x and ε_y are small strains in both the x and y axes, respectively. Due to the isotropic symmetry of 2D materials, we assume $b_1 = b_2$.[36,44] Thus, the in-plane stiffness Y_{2D} was derived as:

$$Y_{2D} = (1/A_0)(2b_1 - b_3^2/2b_1), \quad (6)$$

the elastic constants can be calculated with: $C_{11} = 2b_1/A_0$, $C_{12} = b_3/A_0$. This widely recognized approach, as applied in previous studies,[33–35,45] has been used to determine the mechanical characteristics of the VS_2/graphene composite. The results of the calculated elastic constant (C_{11}, C_{22}, C_{12}) for the VS_2/Gr composite are listed in Table 2. These results meet the Born stability conditions, where $C_{11} > 0$ and $C_{11} - |C_{12}| > 0$, verifying the mechanical stability of the VS_2/Gr composite. As a result of the interaction between VS_2 and graphene, the in-plane stiffness (Y_{2D} = 486.16 N m^{-1}) is significantly higher than that of pure graphene (340 ± 50 N m^{-1})[34,36,39,46] and monolayer VS_2 (80 ± 30 N m^{-1}).[32,44,47] Additionally, the VS_2/Gr composite exhibits a higher in-plane stiffness than many other 2D composite materials (Table 1). The enhanced mechanical strength of the VS_2/graphene composite prevents electrode cracking and mitigates volume expansion, ensuring long-term cycling stability while also suppressing lithium/sodium dendrite formation, which improves battery lifespan and energy density. These properties make VS_2/graphene a highly promising negative electrode material for next-generation LIBs and SIBs.

3.3.2 Mechanical flexibility behaviour. To investigate the mechanical deformation characteristics of the VS_2/G composite, we analyzed its elastic and plastic behavior under uniaxial tensile strain ranging from 0 to +27% in 2.5% increments. The strain was consistently applied along both the armchair and zigzag directions using DFT, while transverse stress was minimized to ensure accurate representation of the material's response along the loading direction. Our findings reveal a linear stress–strain relationship up to 15% strain in both directions, indicative of the elastic region where deformation is fully reversible as illustrated in Fig. 5. In this region, the VS_2/Gr composite retains its original state, known as the harmonic region (ε = 0) when the strain is removed. Beyond 15% strain, distinct mechanical behaviors emerge in the two directions. The armchair direction exhibits brittle behavior, characterized by higher tensile strength but a sharp failure at 17.5% strain, indicating limited plastic deformation. In contrast, the zigzag direction demonstrates ductile behavior, with lower tensile strength but higher strain tolerance, failing at 27.5% strain, which suggests enhanced plasticity before fracture. These differences reflect the intrinsic anisotropy of 2D materials, shaped by their atomic arrangements and bonding orientations. The VS_2/Gr composite is significantly more resilient than pristine graphene, which typically fractures at around 15% strain in the armchair direction and between 16% to 17% in the zigzag direction.[53–55] Furthermore, the fracture strain of VS_2/Gr surpasses that of other composites, such as MoS_2/Gr, which fractures at 13.2% strain.[56] This remarkable improvement highlights the synergistic effect of combining VS_2 with graphene, resulting in a material with excellent mechanical robustness, stretchability, and flexibility.

Table 1 Elastic constants C and in-plane stiffness Y_{2D} for various 2D structures. Both C and Y_{2D} are expressed in N m^{-1}

System	C_{11}	C_{22}	C_{12}	Y_{2D}	Ref.
Gr	349.6	349.6	61.4	338.8	This work
	—	—	—	341.0	33
	—	—	—	340 ± 50	46
	372.5	—	74.5	357.6	36
	—	—	—	335	34
	—	—	—	350	39
VS_2	96.1	93.7	10.9	94.84	This work
	96.0	96.0	28	87.5	15
	—	—	—	88.5	32
	95	—	16	93	47
	171	—	35	—	48
1T-VS_2/Gr	486.9	487.1	19.9	486.1	This work
2H-VS_2/Gr	452.2	452.2	88.4	434.9	15
T-VS_2/BlueP	184	—	26	180	47
H-VS_2/BlueP	193	—	43	187	47
P/G	464	350	—	—	39
2H-MoS_2/Gr	450	—	—	—	15
1T-MoS_2/Gr	492.4	—	—	—	49
BAs/Gr	382	56	—	476	50
Gr/WS_2	479.5	479.5	88.8	463.1	51
BlackP/GDY	261.8	178.7	85.2	—	52

3.4 Electrochemical properties

3.4.1 Li/Na atom adsorption on the VS_2/Gr composite. A systematic study was conducted to analyze the adsorption characteristics of Li and Na atoms on the VS_2/Gr composite. Considering two primary adsorption modes: (i) surface adsorption on the outer layer of VS_2 and (ii) intercalation into the interlayer space between VS_2 and graphene. To identify the most energetically favorable adsorption sites, six configurations were examined: Tv, Ts, Th, Bv, Bs, and Bh as illustrated in Fig. 6.

These correspond to specific adsorption sites including Tv (positioned above the V atom) and Ts (situated above the S atom), Th (hollow site over the triazine ring), Bv (below the V atom in the interlayer), Bs (below the S atom in the interlayer), and Bh (hollow site over the triazine ring). The adsorption energies (E_{ad}) for these sites were computed using the equation:[15]

$$E_{ad} = E_{system+ions} - E_{system} - nE_{ion} \quad (7)$$

where $E_{system+ions}$ and E_{system} denote the total energies of the VS_2/Gr composite in the presence and absence of adsorbed ions, respectively. E_{ion} corresponds to the energy of a single isolated Li/Na atom, while n represents the count of adsorbed ions.

As described by eqn (7), a lower adsorption energy value signifies a stronger interaction between the Li^+/Na^+ and the VS_2/Gr composite, whereas a positive adsorption energy implies the formation of a Li/Na metal cluster instead of effective adsorption. Table 2 presents the computed adsorption energies (E_{ad}), highlighting distinct site preferences for Li^+/Na^+. For Li, the magnitude of adsorption energy $|E_{ad}|$ follows the sequence:

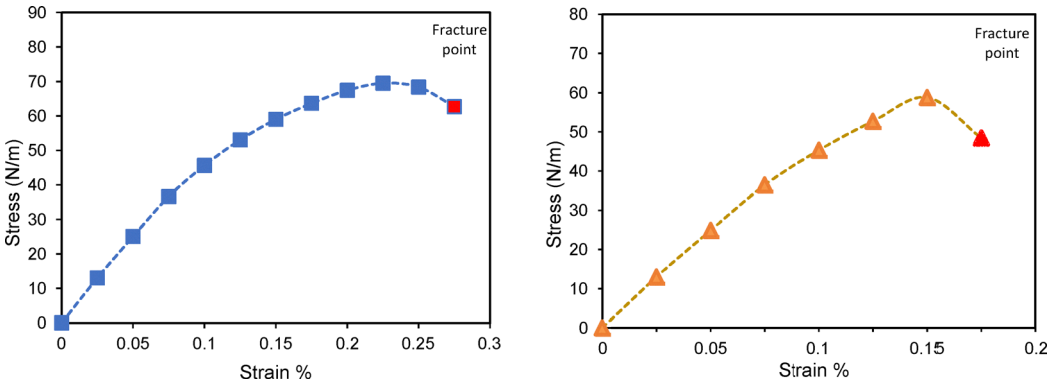

Fig. 5 The uniaxial stress–strain behavior of the VS_2/Gr composite when subjected to tensile strain along the armchair and zigzag orientations.

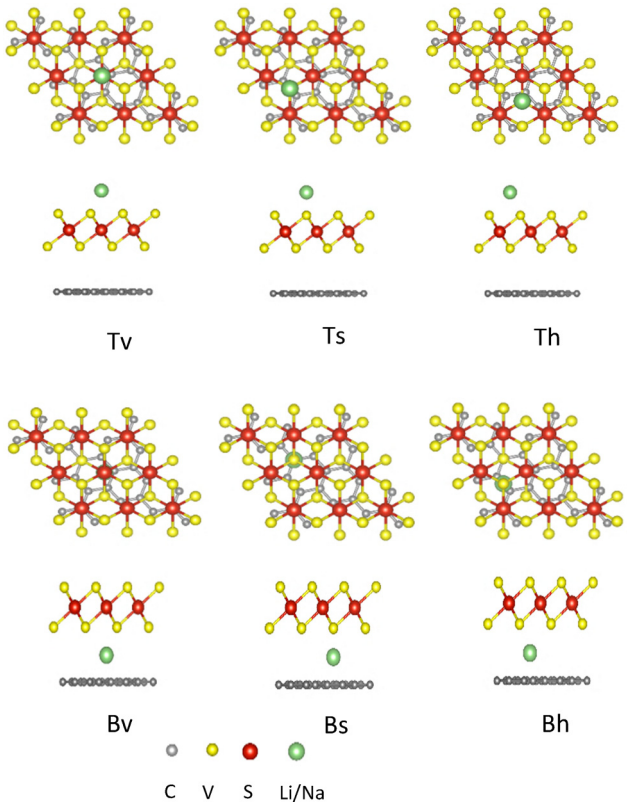

Fig. 6 The adsorption configurations for both Ion/VS_2/Gr and VS_2/Ion/Gr systems, providing a detailed view of the structural characteristics of each adsorption site.

Table 2 The calculated adsorption energy (E_{ad}) for a single adsorbed ion (Li or Na) and the corresponding charge transfer (Δq) associated with these ions

	Li			Na		
System	Adsorption site	Charge (e^-)	E_{ad}	Adsorption site	Charge (e^-)	E_{ad}
Ion/VS_2/Gr	TV	0.880	−1.558	TV	0.865	−1.418
	TS	0.919	−0.625	TH	0.863	−1.395
	TH	0.887	−1.440	TS	0.862	−1.398
VS_2/Ion/Gr	BV	0.885	−1.904	BV	0.869	−1.696
	BS	0.900	−1.194	BS	0.886	−1.194
	BH	0.888	−1.805	BH	0.869	−1.677

Li/VS_2/Gr < VS_2/Li/Gr. Similarly, for Na, the trend is: Na/VS_2/Gr < VS_2/Na/Gr. These trends indicate that both Li/Na atoms preferentially intercalate into the interlayer space rather than adsorb directly onto the VS_2 surface. From Table 2, the most stable adsorption sites for both Li and Na were identified as Bv, Bh, and Tv, with corresponding adsorption energies of E_{ad} = −1.904 eV (Bv), −1.805 eV (Bh), −1.558 eV (Tv) for Li, and E_{ad} = −1.696 eV (Bv), −1.677 eV (Bh), and −1.696 eV (Tv) for Na. These results highlight the strong intercalation tendency of Li and Na within the VS_2/Gr system, significantly influencing their storage and diffusion characteristics. Using the Bader charge analysis method,[57] it was found that both Li/Na atoms transfer approximately 1.0e^- per atom to the VS_2/Gr composite upon adsorption, resulting in their transition to cationic states. This substantial charge transfer confirms a predominantly ionic interaction between the adsorbed ions and the composite. Furthermore, the VS_2/graphene system significantly enhances the bonding strength of Li^+/Na^+ compared to pristine VS_2 or graphene alone. This enhancement is attributed to the synergistic interaction between VS_2 and graphene, which optimizes both the adsorption and intercalation processes. These properties make the VS_2/Gr composite a highly promising candidate for energy storage applications, particularly for lithium- and sodium-ion batteries.

3.4.2 Analysis of electron localization function and charge density. The electron localization function (ELF) is a powerful tool for visualizing the spatial distribution of electrons and understanding the nature of chemical bonding within a material. According to Becke and Edgecombe,[58] ELF enables the identification of localized electron regions, such as bonding pairs, lone pairs, and core electrons, thus helping distinguish between covalent, metallic, and ionic interactions.[59] In the ELF plots of the fully lithiated and sodiated VS_2/graphene systems (Fig. 7), distinct regions of high ELF values (approaching 1.0, shown in red) are observed between V and S atoms, confirming strong covalent bonding. Notably, red regions are also detected within the graphene layer, suggesting some degree of electron localization, which may be associated with the π-electron

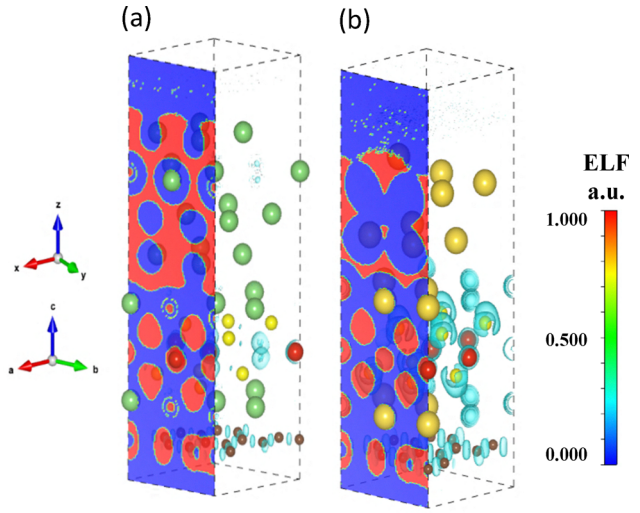

Fig. 7 Electron localization function (ELF) plots at full adsorption capacity for (a) Li–VS_2/Gr and (b) Na–VS_2/Gr heterostructures. Red regions indicate high electron localization (electron-rich zones), while blue regions correspond to low localization (electron-depleted zones). The left panels display ELF isosurfaces, and the right panels show the corresponding atomic configurations.

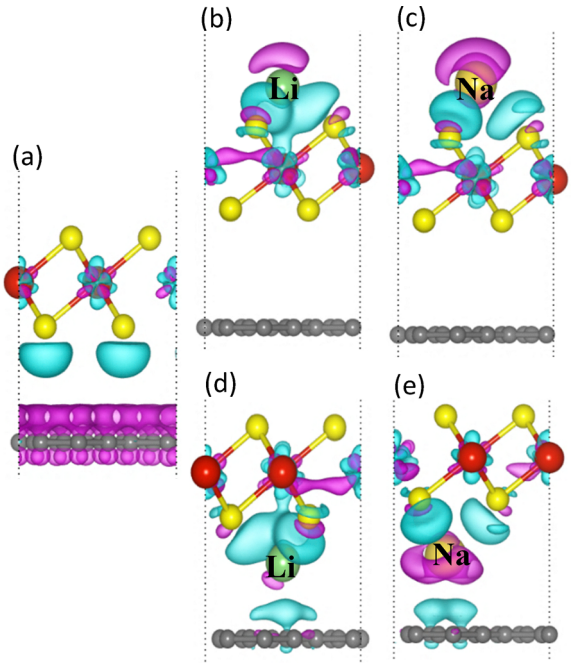

Fig. 8 Charge density difference plots illustrating the most favorable adsorption configurations of a single Li or Na atom. (a) Pristine VS_2/Gr heterostructure; (b) and (c) adsorption on the outer surface of the VS_2 layer; (d) and (e) intercalation within the interlayer region of the VS_2/graphene heterostructure. Cyan and magenta regions represent electron accumulation and depletion, respectively.

system or weak covalent character induced by interaction with the VS_2 layer. In contrast, the ELF distribution around the Li and Na atoms is less localized (ELF < 0.5), indicating predominantly ionic interactions with nearby S or C atoms. These results suggest that while the VS_2 framework maintains strong covalent integrity, the alkali ions (Li/Na) interact with the heterostructure mainly through ionic bonding. Such bonding characteristics are beneficial for accommodating high ion capacities while preserving structural and electronic stability, further supporting the suitability of VS_2/graphene as a robust anode material for Li- and Na-ion batteries.

To investigate the charge transfer behavior during Li/Na adsorption at various sites, the charge density difference was computed using the following equation:[42]

$$\Delta\rho = \rho_{\text{system+ions}} - \rho_{\text{system}} - \rho_{\text{ion}}$$

where $\rho_{\text{system+ions}}$, ρ_{system}, and ρ_{ion} represent the total charge density of the ion-adsorbed system, the pristine VS_2/graphene heterostructure, and the isolated Li or Na atom, respectively. The charge density difference plots reveal significant electron redistribution upon Li or Na incorporation into the heterostructure. In both Ion/VS_2/Gr and VS_2/Ion/Gr configurations, there is evident electron depletion around the Li/Na atoms and accumulation near adjacent sulfur and carbon atoms. A strong interfacial electronic coupling is suggested by the charge buildup between the VS_2 and graphene layers in the VS_2/Ion/Gr configuration, while charge localization around sulfur atoms is observed when ions are adsorbed on the outer surface of VS_2. These findings highlight robust ionic interactions that help prevent Li/Na clustering and improve the system's structural integrity. As shown in Fig. 8, such charge redistribution confirms the stable and favorable interaction of both Li and Na ions with the VS_2/Gr heterostructure, supporting its potential as a high-performance anode material for lithium- and sodium-ion batteries.

3.4.3 Diffusion characteristics of VS_2/graphene. The movement of Li and Na ions is a key factor in defining the charge/discharge rate efficiency of rechargeable batteries.[43]

Faster ion mobility, enabled by lower diffusion energy barriers, significantly enhances the rate performance.

To evaluate this, the climbing image nudged elastic band (CI-NEB) method was employed to examine the migration energy barriers of Li and Na ions in the VS_2/Gr system.[37] For each Li/Na cation diffusion pathway, seven images, including the initial and final configurations, were used in the CI-NEB (climbing image nudged elastic band) calculations. The saddle point, representing the highest energy along the diffusion path, was identified to determine the migration barrier. This diffusion barrier is defined as the energy difference between the saddle point and the most stable configuration. A force convergence criterion of 0.05 eV $Å^{-1}$ was employed to ensure precise optimization of the diffusion pathways. Adsorption analysis revealed three distinct diffusion routes: (i) Bh–Bh, located in the interlayer region; (ii) Bv–Bv, also within the interlayer; and (iii) Tv–Tv, across the external VS_2 surface, as depicted in Fig. 9a. The starting and ending points of these pathways align with the most energetically favorable adsorption configurations for Li and Na, as depicted in Fig. 9b. Fig. 9c illustrates the migration energy barriers for Li and Na diffusion, respectively, confirming that the Bh pathway consistently exhibits the lowest barrier for both ions. Specifically, for

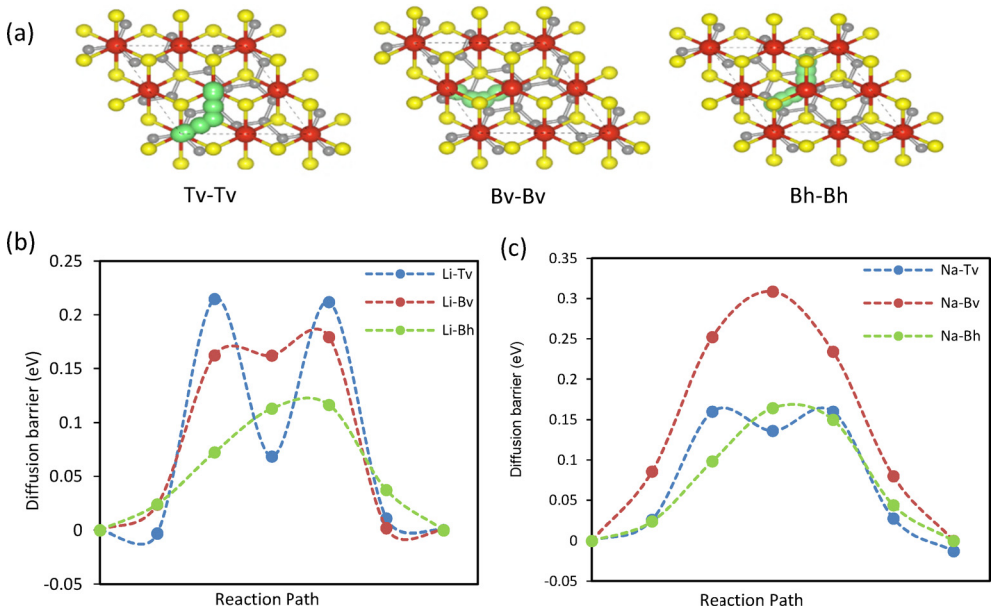

Fig. 9 (a) Diffusion pathways of Li^+/Na^+ across the outer layer and interlayer regions of VS_2/graphene. (b) and (c) Energy barrier profiles for Li and Na ion diffusion across the three evaluated pathways.

Li ions, the Bh pathway demonstrates an exceptionally low diffusion barrier of 0.11 eV, whereas the Tv pathway presents the highest barrier at 0.21 eV. Similarly, for Na ions, the Bh pathway offers the lowest barrier at 0.16 eV, while the Bv pathway reaches 0.3 eV. These results establish the Bh pathway as the most energetically favorable diffusion route, enabling superior ion mobility and contributing to the excellent rate efficiency of VS_2/Gr as an anode component in Li and Na batteries. Furthermore, the migration diffusion energy barrier for Li within VS_2/Gr (0.11 eV) is significantly lower than in pristine VS_2 (0.22 eV)[15,43] and graphene (0.37 eV),[60] demonstrating the impact of the composite in reducing diffusion resistance. Likewise, Na diffusion in VS_2/Gr (0.16 eV) is considerably lower than in pristine VS_2 (0.63 eV),[14] confirming the effectiveness of the composite in facilitating Na-ion transport. These findings underscore the synergistic effect of VS_2/Gr in lowering the ion diffusion barriers, thereby improving overall electrochemical performance. The significantly reduced migration energy barriers along the Bh pathway highlight the outstanding capability of VS_2/Gr for fast-charging rechargeable batteries, solidifying its suitability as an efficient optimized electrode for both Li and Na ion storage. These exceptionally high values highlight the superior ion transport capabilities of the VS_2/Gr, surpassing many others. To further evaluate ion diffusivity at 300 K, the diffusion coefficients for Li^+ and Na^+ were determined using eqn (4), yielding values of 5.42×10^{-5} cm^2 s^{-1} and 5.32×10^{-6} cm^2 s^{-1}, respectively. 2D negative electrode materials designed for LIBs and SIBs. For comparison, graphene demonstrates a significantly lower diffusion coefficient of 2.0×10^{-11} cm^2 s^{-1} for Li^+,[51] while other composites, such as WS_2/graphene ($5.54.2 \times 10^{-10}$ cm^2 s^{-1} for Li^+),[61] C_2N/graphene (2.97×10^{-11} cm^2 s^{-1} for Li^+),[62] and boron arsenide/graphene (BAs/Gr) (1.27×10^{-10} cm^2 s^{-1} for Li^+),[50] exhibit comparatively lower diffusivity. The ultra-high diffusion coefficients of Li and Na within the VS_2/Gr system establish it as a high-rate negative electrode material for LIBs and SIBs ensuring rapid ion transport and enhanced electrochemical performance during charge–discharge cycling.

3.4.4 Average open-circuit voltage and theoretical specific capacity. In rechargeable batteries, open-circuit voltage (V_{OC}) and theoretical specific capacity (C_s) are critical factors in determining the electrochemical efficiency of electrode materials. This study evaluates the C_s and V_{OC} based on a $2 \times 2 \times 1$ VS_2/Gr supercell, where Li/Na atoms are sequentially inserted into both the interlayer region and the outer surface of the composite. Individually, the charge/discharge mechanism adheres to the half-cell reaction:

$$VS_2/Gr + xIon^+ + xe^- \leftrightarrow Ion_xVS_2/Gr \quad (Ion = Li, Na),$$

where x denotes the number of intercalated Li/Na atoms. The V_{OC} is determined by computing the DFT total energies before and after Li^+/Na^+ intercalation. Since entropy and volume effects are generally negligible during the electrochemical reaction, the V_{OC} is calculated using the following equation:[15,63]

$$V_{OC} = -\frac{E_{system+ion} - E_{system} - x \cdot E_{ion}}{cx \cdot e} \quad (8)$$

where $E_{system+ion}$ and E_{system} are the total energies of Ion_xVS_2/Gr and VS_2/Gr, respectively, E_{ion} represents the energy per atom of the bulk metal (Li/Na), and x is the number of intercalated Li/Na atoms. A negative adsorption energy (E_{ad}) indicates that the Li and Na atoms can still be intercalated into the material. The intercalation process continues until E_{ad} becomes positive, suggesting that no additional Li/Na atoms can be accommodated, leading to ion clustering. The maximum theoretical

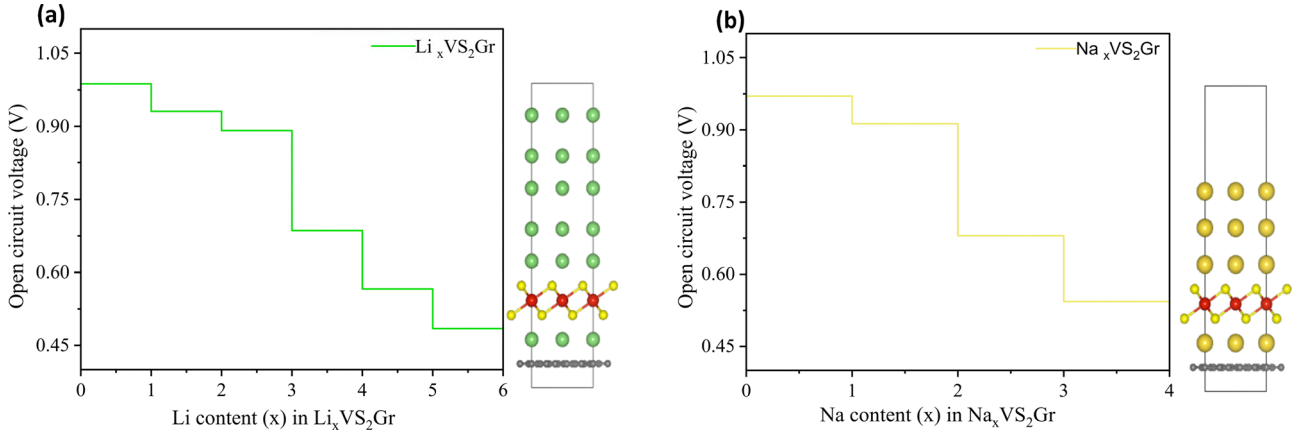

Fig. 10 Computed voltage profile of (a) Li-intercalated VS_2/Gr relative to Li/Li^+ and (b) Na-intercalated VS_2/Gr relative to Na/Na^+.

capacity is then determined using the equation:[14,43,63–65]

$$C_s = z \cdot x_{max} \cdot \frac{F}{M_{VS_2/Gr}} \quad (9)$$

where x represents the maximum concentrations of the inserted Li/Na atoms, z is the valence number (z = 1 for Li and Na), F is the Faraday constant (26 801 mAh mol^{-1}), and $M_{VS_2/Gr}$ is the molar mass of the VS_2/Gr unit cell. As illustrated in Fig. 10a, increasing the Li concentration from x = 0 to x = 6, the V_{OC} gradually decreases from 0.98 to 0.48 V, yielding an average V_{OC} of 0.75 V for Li_xVS_2/Gr. Similarly, for Na intercalation (Fig. 10b), the voltage profile ranges from 0.97 to 0.54 V, with an average V_{OC} of 0.77 V for Na_xVS_2/Gr as the Na concentration increases from x = 0 to x = 4. A lower V_{OC} suggests strong interactions between the inserted ions (Li^+ or Na^+) and the host material, indicating that the material can effectively accommodate and retain ions. This enhances the battery's energy storage capability and improves overall performance, meaning that the material exhibits higher specific capacity. Furthermore, the discrete steps in the V_{OC} decrease rather than an abrupt drop suggest a stable and controlled intercalation process. Since an ideal anode material must possess a low V_{OC}, our results show that the VS_2/Gr composite is a viable negative electrode material candidate for both Li^+/Na^+ electrochemical storage devices. Furthermore, the maximum specific capacities of the VS_2/Gr composite for Li and Na storage were calculated as 1156 mAh g^{-1} and 770 mAh g^{-1}, respectively. The observed values indicate a significant improvement in comparison to pure graphene (372 mAh g^{-1}) and VS_2 (466 mAh g^{-1} for Li, 233 mAh g^{-1} for Na).[15] The lower capacity observed for Na-ion storage compared to Li-ion storage is attributed to the larger effective ionic radius of Na^+ ions, which limits its accommodation within the VS_2/Gr interlayers. This behavior aligns with previous studies on Na-ion intercalation limitations as illustrated in Table 3. Addition to the VS_2/Gr composite exhibits superior electrochemical performance compared to pristine VS_2 and graphene, theoretical capacity of VS_2/graphene is higher than other 2D materials due to a higher capacity, a lower average open-circuit voltage and a reduced Li^+/Na^+ diffusion barrier as shown in Table 3. Although VS_2/BlueP exhibits a slightly higher capacity, it suffers from a higher diffusion barrier, making VS_2/Gr a more favorable choice for efficient Li^+/Na^+ storage.

Table 3 Comparison of theoretical specific capacity (C_s) in mAh g^{-1} of various 2D composites for LIBs and SIBs

Ion battery type	Materials	C_s	Ref.
LIBs	$1TVS_2$/Gr	1156	This work
	VS_2/BlueP	1211	47
	Vertical VS_2/Gr	989	66
	$1HVS_2$/Gr	771	15
	$1TVS_2$	466	32
	MoS_2/WS_2	137	67
	V_2CO_2/Gr	234	68
	WS_2/Gr	714	69
	$NbSe_2$/Gr	1000	70
	WSe_2/Gr	744	71
	C_2N/Gr	490	62
	VS_2	466	13
	VS_4/rGO	1105	72
	VS_2 (2H and 1T)/Gr	569	8
	P/Gr	485.3	39
	Gr/BAs	920	50
	BlackP/GDY	384.7	52
SIBs	$1TVS_2$/Gr	770	This work
	$1HVS_2$	232.9	14
	HollowVS_2/RGO	430	26
	$1TVS_2$	116.4	14
	$1TVS_2$	466	32
	$1HVS_2$/Gr	578	15
	MoS_2/VS_2	584	73
	WS_2/Gr	590	74
	WSe_2/Gr	300	75
	P/Gr	580	12

4. Conclusion

Through first-principles simulations, we carried out a systematic investigation of the VS_2/Gr composite and its electrochemical potential as an anode material for Li^+/Na^+ electrochemical storage devices. Our findings show that the VS_2/Gr exhibits exceptional structural stability with a negative formation energy

of −0.011 eV, indicating its thermodynamic favorability. For electronic properties, VS_2/Gr maintains metallic characteristics due to the strong contribution of V-d and S-p orbitals near the Fermi level, ensuring high electronic conductivity. Mechanically, the VS_2/Gr demonstrates higher stiffness compared to pristine graphene and VS_2, with an elastic constant (C_{11} = 349.65, C_{22} = 349.65, C_{12} = 61.43), confirming its mechanical stability. Due to the synergistic effect between VS_2 and graphene, its in-plane stiffness (Y_{2D} = 486.16 N m^{-1}) surpasses that of pristine graphene and monolayer VS_2, making it one of the most mechanically robust 2D composites. Regarding mechanical flexibility, VS_2/Gr exhibits anisotropic behaviour under tensile strain, remaining elastic up to 15% strain. Beyond this, it shows brittle failure in the armchair direction at 17.5% strain and ductile behaviour in the zigzag direction, failing at 27.5% strain, indicating enhanced flexibility and stretchability.

For electrochemical performance, the VS_2/Gr composite offers an exceptionally low ion diffusion barrier, with Li ions exhibiting a migration energy barrier of 0.11 eV and Na ions 0.16 eV, facilitating fast charge/discharge rates. The open circuit voltage (V_{OC}) profiles indicate stable ion storage, with an average V_{OC} of 0.75 V for Li-ions and 0.77 V for Na-ions, indicating that the material can effectively accommodate and retain ions. Furthermore, VS_2/Gr demonstrates remarkable energy storage capacity, achieving a maximum specific capacity of 1156 mAh g^{-1} for Li-ion storage and 770 mAh g^{-1} for Na-ion storage. The lower capacity for Na storage is attributed to the larger ionic radius of Na^+, which limits its accommodation within the interlayers. In summary, the VS_2/Gr composite emerges as a highly promising optimized electrode for next-generation LIBs and NIBs. Its high capacity, low diffusion barriers, and stable voltage profiles highlight its potential for efficient and high-performance energy storage applications.

Conflicts of interest

There are no conflicts to declare.

Data availability

The data supporting the findings of this study are publicly available in the Zenodo repository at the following DOI: **https://doi.org/10.5281/zenodo.15332576**.

Acknowledgements

The authors wish to acknowledge the financial support provided through the Fundamental Research Grant Scheme (FRGS), project no. FRGS/1/2020/STG07/UPM/02/2 by Ministry of Higher Education Malaysia.

References

1 S. J. Lee, J. Theerthagiri, P. Nithyadharseni, P. Arunachalam, D. Balaji, A. M. Kumar, J. Madhavan, V. Mittal and M. Y. Choi, *Renewable Sustainable Energy Rev.*, 2021, **143**, 110849.
2 B. M. Khan, W. C. Oh, P. Nuengmatch and K. Ullah, *Mater. Sci. Eng., B*, 2023, **287**, 116141.
3 A. J. Hassan, *Iran J. Org. Chem.*, 2019, **11**, 2659–2665.
4 X. He, R. Wang, H. Yin, Y. Zhang, W. Chen and S. Huang, *Appl. Surf. Sci.*, 2022, **584**, 152537.
5 J. Khan, S. Khalid, W. Uddin, R. Khenata, M. Khan, S. U. Rehman, M. Ahmad, S. Wang, W. Huang and S. B. Omran, *J. Mater. Res. Technol.*, 2021, **11**, 1672–1677.
6 G. Dong, Y. Fang, S. Liao, K. Zhu, J. Yan, K. Ye, G. Wang and D. Cao, *J. Colloid Interface Sci.*, 2021, **601**, 594–603.
7 A. S. Dobrota, I. A. Pašti, S. V. Mentus, B. Johansson and N. V. Skorodumova, *Electrochim. Acta*, 2017, **250**, 185–195.
8 N. S. Mikhaleva, M. A. Visotin, A. A. Kuzubov and Z. I. Popov, *J. Phys. Chem. C*, 2017, **121**, 24179–24184.
9 H. Qin, Z. Mo, J. Lu, X. Sui, Z. Song, B. Chen, Y. Zhang, Z. Zhang, X. Lei and A. Lu, *Carbon*, 2024, **216**, 118559.
10 H. Chen, X. Li, H. Liu, J. Chen and Z. Shi, *Chem. Eng. Sci.*, 2024, **298**, 120335.
11 S. Goriparti, E. Miele, F. De Angelis, E. Di Fabrizio, R. P. Zaccaria and C. Capiglia, *J. Power Sources*, 2014, **257**, 421–443.
12 Z. Mansouri, A. Sibari, A. Al-Shami, S. Lahbabi, A. El Kenz, A. Benyoussef, A. El Fatimy and O. Mounkachi, *Comput. Mater. Sci.*, 2022, **202**, 110936.
13 Y. Jing, Z. Zhou, C. R. Cabrera and Z. Chen, *J. Phys. Chem. C*, 2013, **117**, 25409–25413.
14 D. B. Putungan, S.-H. Lin and J.-L. Kuo, *ACS Appl. Mater. Interfaces*, 2016, **8**, 18754–18762.
15 B. Liu, T. Gao, P. Liao, Y. Wen, M. Yao, S. Shi and W. Zhang, *Phys. Chem. Chem. Phys.*, 2021, **23**, 18784–18793.
16 E. Pomerantseva and Y. Gogotsi, *Nat. Energy*, 2017, **2**, 1–6.
17 R. Frisenda, E. Navarro-Moratalla, P. Gant, D. P. De Lara, P. Jarillo-Herrero, R. V. Gorbachev and A. Castellanos-Gomez, *Chem. Soc. Rev.*, 2018, **47**, 53–68.
18 Y. Liu, N. O. Weiss, X. Duan, H.-C. Cheng, Y. Huang and X. Duan, *Nat. Rev. Mater.*, 2016, **1**, 1–17.
19 Y. Li, F. Wu, H. Zhang, W. Wei, H. Jiang and C. Deng, *Carbon*, 2023, **203**, 571–579.
20 A. Massaro, A. Pecoraro, A. B. Muñoz-García and M. Pavone, *J. Phys. Chem. C*, 2021, **125**, 2276–2286.
21 X. Li, J. Zhang, Z. Liu, C. Fu and C. Niu, *J. Alloys Compd.*, 2018, **766**, 656–662.
22 H. Yuan, J. Zhao, Q. Wang, D. Manoj, A. Zhao, K. Chi, J. Ren, W. He, Y. Zhang and Y. Sun, *ACS Appl. Mater. Interfaces*, 2020, **12**, 15507–15516.
23 W. Zhang, X. Chen, J. Zhang, C. Tuo, L. Ji, H. Li, X. Zhang and F. Yang, *Int. J. Hydrogen Energy*, 2018, **43**, 22949–22954.
24 G. Yang, B. Zhang, J. Feng, H. Wang, M. Ma, K. Huang, J. Liu, S. Madhavi, Z. Shen and Y. Huang, *ACS Appl. Mater. Interfaces*, 2018, **10**, 14727–14734.
25 D. Wu, C. Wang, M. Wu, Y. Chao, P. He and J. Ma, *J. Energy Chem.*, 2020, **43**, 24–32.
26 H. Qi, L. Wang, T. Zuo, S. Deng, Q. Li, Z. H. Liu, P. Hu and X. He, *ChemElectroChem*, 2020, **7**, 78–85.

27 P. Giannozzi, S. Baroni, N. Bonini, M. Calandra, R. Car, C. Cavazzoni, D. Ceresoli, G. L. Chiarotti, M. Cococcioni, I. Dabo, A. Dal Corso, S. de Gironcoli, S. Fabris, G. Fratesi, R. Gebauer, U. Gerstmann, C. Gougoussis, A. Kokalj, M. Lazzeri, L. Martin-Samos, N. Marzari, F. Mauri, R. Mazzarello, S. Paolini, A. Pasquarello, L. Paulatto, C. Sbraccia, S. Scandolo, G. Sclauzero, A. P. Seitsonen, A. Smogunov, P. Umari and R. M. Wentzcovitch, *J. Phys.: Condens. Matter*, 2009, **21**, 395502.
28 J. P. Perdew, K. Burke and M. Ernzerhof, *Phys. Rev. Lett.*, 1996, **77**, 3865.
29 K. Momma and F. Izumi, *Appl. Crystallogr.*, 2011, **44**, 1272–1276.
30 S. Grimme, *J. Comput. Chem.*, 2006, **27**, 1787–1799.
31 N. E. Benti, G. A. Tiruye and Y. S. Mekonnen, *RSC Adv.*, 2020, **10**, 21387–21398.
32 M. Salavati and T. Rabczuk, *Comput. Mater. Sci.*, 2019, **160**, 360–367.
33 A. R. Puigdollers, G. Alonso and P. Gamallo, *Carbon*, 2016, **96**, 879–887.
34 M. Topsakal, S. Cahangirov and S. Ciraci, *Appl. Phys. Lett.*, 2010, **96**, 091912.
35 R. Majidi, *Theor. Chem. Acc.*, 2017, **136**, 109.
36 L. Ye, S. Wu and Z. Wang, *J. Electron. Mater.*, 2020, **49**, 5713–5720.
37 G. Henkelman, B. P. Uberuaga and H. Jónsson, *J. Chem. Phys.*, 2000, **113**, 9901–9904.
38 P. Hirunsit, M. Liangruksa and P. Khanchaitit, *Carbon*, 2016, **108**, 7–20.
39 G.-C. Guo, D. Wang, X.-L. Wei, Q. Zhang, H. Liu, W.-M. Lau and L.-M. Liu, *J. Phys. Chem. Lett.*, 2015, **6**, 5002–5008.
40 Z. Popov, N. Mikhaleva, M. Visotin, A. Kuzubov, S. Entani, H. Naramoto, S. Sakai, P. Sorokin and P. Avramov, *Phys. Chem. Chem. Phys.*, 2016, **18**, 33047–33052.
41 P. Zhang, Y. Wang, W. Lei, Y. Zou, W. Jiang, Z. Ma and C. Lu, *ACS Appl. Mater. Interfaces*, 2019, **11**, 24648–24658.
42 Y. Cui, W. Fan, X. Liu, J. Ren and Y. Gao, *Comput. Mater. Sci.*, 2021, **200**, 110767.
43 Y. Cui, W. Fan, Y. Ren, G. Yang and Y. Gao, *Prog. Nat. Sci.: Mater. Int.*, 2022, **32**, 236–241.
44 W. Shi and Z. Wang, *J. Phys.: Condens. Matter*, 2018, **30**, 215301.
45 R. C. Andrew, R. E. Mapasha, A. M. Ukpong and N. Chetty, *Phys. Rev. B: Condens. Matter Mater. Phys.*, 2012, **85**, 125428.
46 C. Lee, X. Wei, J. W. Kysar and J. Hone, *Science*, 2008, **321**, 385–388.
47 H. Lin, X. Jin, N. Lou, D. Yang, R. Jin and Y. Huang, *Appl. Surf. Sci.*, 2020, **533**, 147478.
48 C. M. Bastos, R. Besse, J. L. Da Silva and G. M. Sipahi, *Phys. Rev. Mater.*, 2019, **3**, 044002.
49 S. Singh, C. Espejo and A. H. Romero, *Phys. Rev. B*, 2018, **98**, 155309.
50 Y. Guan, G. Huang, X. Li and L. Zhang, *Diamond Relat. Mater.*, 2024, **147**, 111365.
51 M. Zhang, C. Tang, W. Cheng and L. Fu, *J. Alloys Compd.*, 2021, **855**, 157432.
52 F. Yang, D. Li, S. Jiang, S. Lou, W. Wang and B. Hu, *Comput. Mater. Sci.*, 2024, **241**, 113059.
53 C. Daniels, A. Horning, A. Phillips, D. V. Massote, L. Liang, Z. Bullard, B. G. Sumpter and V. Meunier, *J. Phys.: Condens. Matter*, 2015, **27**, 373002.
54 N. Fan, Z. Ren and G. Jing, *Materials*, 2017, **10**, 164.
55 B. Mortazavi, *Carbon*, 2017, **118**, 25–34.
56 N. Ghobadi, *Curr. Appl. Phys.*, 2017, **17**, 1483–1493.
57 R. F. Bader, *Acc. Chem. Res.*, 1985, **18**, 9–15.
58 A. D. Becke and K. E. Edgecombe, *J. Chem. Phys.*, 1990, **92**, 5397–5403.
59 J. K. Burdett and T. A. McCormick, *J. Phys. Chem. A*, 1998, **102**, 6366–6372.
60 E. Pollak, B. Geng, K.-J. Jeon, I. T. Lucas, T. J. Richardson, F. Wang and R. Kostecki, *Nano Lett.*, 2010, **10**, 3386–3388.
61 K. Toyoura, Y. Koyama, A. Kuwabara and I. Tanaka, *J. Phys. Chem. C*, 2010, **114**, 2375–2379.
62 Y. Ding, B. Xiao, J. Li, Q. Deng, Y. Xu, H. Wang and D. Rao, *J. Phys. Chem. C*, 2019, **123**, 3353–3367.
63 D. Wang, Y. Liu, X. Meng, Y. Wei, Y. Zhao, Q. Pang and G. Chen, *J. Mater. Chem. A*, 2017, **5**, 21370–21377.
64 J. Yang, J. Wang, X. Dong, L. Zhu, D. Hou, W. Zeng and J. Wang, *Appl. Surf. Sci.*, 2021, **544**, 148775.
65 Z. Zhang, M. Yang, N. Zhao, L. Wang and Y. Li, *Phys. Chem. Chem. Phys.*, 2019, **21**, 23441–23446.
66 Z. Huang, X. Han, X. Cui, C. He, J. Zhang, X. Wang, Z. Lin and Y. Yang, *J. Mater. Chem. A*, 2020, **8**, 5882–5889.
67 S. Fan, X. Zou, H. Du, L. Gan, C. Xu, W. Lv, Y.-B. He, Q.-H. Yang, F. Kang and J. Li, *J. Phys. Chem. C*, 2017, **121**, 13599–13605.
68 Y. Aierken, C. Sevik, O. Gülseren, F. M. Peeters and D. Çakır, *J. Mater. Chem. A*, 2018, **6**, 2337–2345.
69 J. Li, H. Yan, W. Wei, X. Li and L. Meng, *ChemElectroChem*, 2018, **5**, 3222–3228.
70 Q. H. Nguyen, H. Kim, I. T. Kim, W. Choi and J. Hur, *Chem. Eng. J.*, 2020, **382**, 122981.
71 X. Wang, J. He, B. Zheng, W. Zhang and Y. Chen, *Electrochim. Acta*, 2018, **283**, 1660–1667.
72 R. C. Sekhar, K. Byeong-Hwan, X. Xiaodong, Y. Jieun, J. H. Young, O. Dorj, P. Noejung, C. Jaephil and S. H. Suk, *J. Am. Chem. Soc.*, 2013, **135**, 8720–8725.
73 A. Samad and Y.-H. Shin, *ACS Appl. Mater. Interfaces*, 2017, **9**, 29942–29949.
74 D. Su, S. Dou and G. Wang, *Chem. Commun.*, 2014, **50**, 4192–4195.
75 J. S. Cho, S.-K. Park, K. M. Jeon, Y. Piao and Y. C. Kang, *Appl. Surf. Sci.*, 2018, **459**, 309–317.